



Facilitated Electron Transfer by Mn dopants in 1-Dimensional CdS Nanorods for Enhanced Photocatalytic Hydrogen Generation

Journal:	<i>Journal of Materials Chemistry A</i>
Manuscript ID	TA-ART-10-2022-008409.R1
Article Type:	Paper
Date Submitted by the Author:	08-Feb-2023
Complete List of Authors:	MacSwain, Walker; Syracuse University Lin, Hanjie; Syracuse University, Chemistry Li, Zhijun; Syracuse University Li, Shuuya; Syracuse University, Chemistry Chu, Chun; Syracuse University, Chemistry Dube, Lacie; Brown University, Chemistry Leem, Gyu; State University of New York College of Environmental Science and Forestry at Syracuse, Chemistry Zheng, Weiwei; Syracuse University, Chemistry

ARTICLE

Facilitated Electron Transfer by Mn dopants in 1-Dimensional CdS Nanorods for Enhanced Photocatalytic Hydrogen Generation

Received 00th January 20xx,
Accepted 00th January 20xx

DOI: 10.1039/x0xx00000x

Walker MacSwain,^a Hanjie Lin,^a Zhi-Jun Li,^a Shuya Li,^a Chun Chu,^a Lacie Dube,^b Ou Chen,^b Gyu Leem,^{c,d} Weiwei Zheng.^{a,*}

Using sunlight to produce hydrogen gas via photocatalytic water splitting is highly desirable for green energy harvesting and sustainability. In this work, Mn²⁺ doped 1-dimensional (1D) CdS nanorods (NRs) with Pt tips (*i.e.*, 1D Mn:CdS-Pt NRs) were synthesized for photocatalytic water splitting to generate hydrogen gas. The incorporation of Mn²⁺ dopants inside the 1D CdS NRs with significantly longer lifetime (\sim ms) than that of host exciton (\sim ns) facilitates charge separation; the electron transfer to metal Pt tips leads to enhanced photocatalytic activity in water splitting redox reactions. The as-synthesized Mn²⁺ doped CdS NR-based photocatalyst generated an order of magnitude greater yield of hydrogen gas compared to the undoped CdS NR-based photocatalyst. The enhanced charge transport from the long lifetime excited state of Mn²⁺ dopants in light harvesting semiconductor nanomaterials present a new opportunity to increase the overall photocatalytic performance.

Introduction

Photocatalytic hydrogen generation by water splitting has drawn a tremendous amount of research interest due to its green nature and promising solution for the world energy crisis.¹ Quantum confined semiconductor nanocrystals (NCs) have excellent optical and electrical properties including large absorption extinction coefficient in the visible range, size- and shape-tunable bandgap, and great photostability. The photogenerated charge carriers (*i.e.*, excited electrons and holes) from NCs can be used for photocatalytic redox reactions, such as photocatalytic water splitting for hydrogen generation. To date, there are multiple semiconductors including metal chalcogenides such as CdS,^{2,3} CdSe,⁴⁻⁶ PbS,⁷ and metal oxides such as ZnO⁸ and TiO₂⁹ that have been developed to split water and generate hydrogen gas. Among these materials, CdS NCs have been heavily utilized due to their \sim 2.4 eV bandgap, which is narrow enough to absorb visible light while still having a conduction band that is sufficiently negative to reduce water to produce hydrogen gas.^{3,10,11} However, the photocatalytic yields of CdS NCs are limited

primarily due to insufficient charge separation as the result of fast exciton recombination (on the order of ns to tens of ns) compared to slower surface catalytic reactions (ms to s).¹¹⁻¹⁴ The insufficient charge separation leads to limited charge carriers (electrons and holes) accessible to photocatalytic redox reactions.

Increased photocatalytic yields of water splitting for H₂ gas generation have been reported from 0-dimensional (0D) CdS QDs of 17 (μ mol/hour/g)¹⁵ to 1D CdS nanorods (NRs) of 60 (μ mol/hour/g)¹⁶ while 2D CdS nanoplatelets have been reported to have 30.3 (μ mol/hour/g),¹⁷ tetrapods \sim 2640 (μ mol/hour/g),¹⁸ cubes 1600 (μ mol/hour/g),¹⁹ and pyramids 4600 (μ mol/hour/g).¹⁸ These increases in reaction yields are due to the slight polarizations when exciting electrons across the unconfined axis or axes, leading to a reduced charge recombination rate.²⁰ Therefore, advanced shaped CdS NCs with enhanced charge separations can increase the efficiency of photocatalytic redox reactions including water splitting.^{12,17,21} Another approach to increasing the charge separation in CdS NCs is by adding a metal co-catalyst, such as Pt,^{12,17,21-23} Au,^{24,25} Ni,^{6,26,27} and Ag,²⁸ with efficient electron transfer from CdS to the metal co-catalyst. The metal co-catalyst acts as a sink for the excited electrons to move into which can increase the charge separation due to a fast rate of electron transfer (\sim ps)²⁵ from the conduction band of CdS to the metal.

Pt nanoparticles (NPs) are widely used as co-catalysts in CdS-based photocatalytic water splitting^{12,17,22,23,29} since Pt can both readily accept electrons to its Fermi energy level and is highly hydrophilic. This innate hydrophilicity increases the possibilities of hydrogen adsorption on the active sites of the Pt co-catalyst, which can increase the likelihood of an excited electron being

^a Department of Chemistry, Syracuse University, Syracuse, New York 13244, United States.

^b Department of Chemistry, Brown University, Providence, Rhode Island, 02912, United States.

^c Department of Chemistry, State University New York College of Environmental Science Forestry, Syracuse, New York 13210, United States.

^d The Michael M. Szwarc Polymer Research Institute, 1 Forestry Drive, Syracuse, New York 13210, United States.

† Electronic Supplementary Information (ESI) available: Experimental Details for ZnS shell coated core/shell NRs, characterization data (TEM and XRD), optical data (absorbance, emission, and PL lifetime) electrochemical data (EIS, CV, photocurrent, and band edge) quantum efficiency calculations, band structures for Mn:CdS/ZnS, and control experiments of photocatalysis (Recycle test, doping concentration and Pt NP size-dependent photocatalytic performance). See DOI: 10.1039/x0xx00000x

involved in photocatalytic water splitting for hydrogen gas generation. Coupled with a light harvesting CdS NC photocatalytic system, Pt co-catalysts have shown significantly higher hydrogen yields among the available co-catalysts.^{12, 17, 21, 23, 29, 30} For example, the photocatalytic water splitting yield of Pt modified CdS NCs have been reported to be 56,000 ($\mu\text{mol}/\text{hour}/\text{g}$)³⁰ while other CdS-based metal co-catalysts have reported 400.6 ($\mu\text{mol}/\text{hour}/\text{g}$) for Au,^{24, 25} 25,484 ($\mu\text{mol}/\text{hour}/\text{g}$) for Ni,²⁶ and 32 ($\mu\text{mol}/\text{hour}/\text{g}$) for Ag.²⁸

However, changing the dimensionality of the CdS photocatalyst and adding a Pt co-catalyst cannot completely overcome the issue of inherent short lifetimes of excitons ($\sim\text{ns}$) even though a portion of charge carriers can transport to the Pt particles before exciton recombination. Doping transition metal ions inside the host semiconductor lattice can provide an additional exciton relaxation pathway by host-to-dopant energy transfer; this is an attractive strategy for increasing catalytic performance as the dopants can alter the dynamics of charge separation and recombination.^{27, 31-34} Manganese (Mn^{2+}) ions are a particularly useful dopant as their orange emission around 600 nm has a long emission lifetime ($\sim\text{ms}$) from the spin forbidden d-d transition (${}^4\text{T}_1$ to ${}^6\text{A}_1$).^{31, 33-37} The ms lifetime of the excited state of Mn^{2+} dopants is much longer (4-6 orders of magnitude higher) than that of the fast decay of excitons of semiconductor NCs (on the order of ns or tens of ns). Therefore, the long lifetime Mn^{2+} dopants can provide a much longer time window for charge transport³⁸ or energy transfer,³⁹ which is on a similar order of magnitude as surface photocatalytic reactions ($\text{ms} - \text{s}$).^{13, 14} Previous studies have demonstrated that doping Mn^{2+} into 0D CdS QDs increases the photocatalysis yield of hydrogen gas from 17 ($\mu\text{mol}/\text{hour}/\text{g}$)¹⁵ in the undoped system to 300 ($\mu\text{mol}/\text{hour}/\text{g}$).³⁸ Therefore, greater charge separation can occur by host-to-dopant energy transfer which can increase the photocatalytic yield.

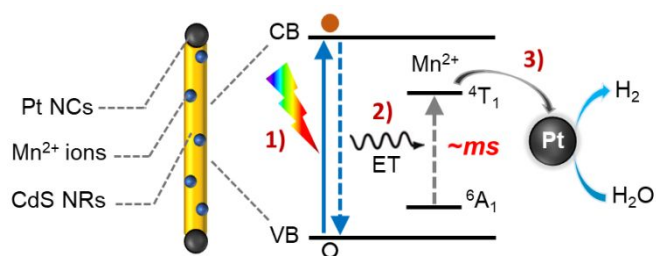


Fig 1. Schematic illustration of the excitonic and energy transfer processes in Mn^{2+} doped CdS NRs with Pt-tips for H_2 generation. 1) Photoexciting an electron from the valence band (VB) to the conduction band (CB), 2) energy transfer (ET) from the host CdS NR to Mn^{2+} dopants, and 3) electron transfer from dopants (with $\sim\text{ms}$ lifetime) to active sites of Pt NP tips for H_2 generation from water splitting.

In this report, we designed a new photocatalyst by doping Mn^{2+} ions into 1D CdS NRs with Pt-tips (*i.e.*, 1D Mn:CdS-Pt NRs) for photocatalytic H_2 generation from water splitting (Figure 1). Following photoexcitation of host CdS NRs to generate excited electrons and holes (step 1 in Figure 1), two-step charge carrier

transport occurs including host-to-dopant energy transfer (step 2 in Figure 1) and electron transfer from Mn^{2+} dopants to Pt NPs (step 3 in Figure 1). The added charge transport pathways mediated by the long lifetime dopants could prevent the fast exciton recombination, leading to enhanced photocatalytic water splitting. Aided by the 4.1 ms Mn^{2+} dopant emission lifetime, compared to the 7.9 ns lifetime of the host 1D CdS NRs, the Mn^{2+} doped 1D CdS NRs can efficiently boost the charge separation and the following electron transportation for photocatalytic water splitting under blue light irradiation. Compared with their undoped counterpart (*i.e.*, 1D CdS-Pt NRs), the water splitting efficiency of Mn:CdS-Pt NRs increased from 64,000 to 287,000 $\mu\text{mol}/\text{hour}/\text{g}$ of hydrogen gas; the yield is increased by 448% (~ 4.5 -fold enhancement). The long lifetime of the dopants can increase charge separation and supply a bridging pathway for efficient photocatalysis on metal co-catalysts, which provide a new opportunity for photocatalytic redox reaction.

EXPERIMENTAL SECTION

Chemicals. Cadmium oxide (CdO, $\geq 99.0\%$, Sigma-Aldrich), sulfur (99.998%, Sigma-Aldrich), 1-tetradecylphosphonic acid (TDPA, 98%, Sigma-Aldrich), trioctylphosphine oxide (TOPO, 99%, Alfa-Aesar), trioctylphosphine (TOP, 90%, Sigma-Aldrich), chloroform (99.8 %, Fisher-Scientific), Mn(II) acetate anhydrous (99.99%, Alfa-Aesar), oleylamine (OAm, 70%, Sigma-Aldrich), oleic acid (OA, 90%, Sigma-Aldrich), 1, 2-dichlorobenzene ($\geq 99\%$, Sigma-Aldrich), diphenyl ether ($\geq 99\%$, Sigma-Aldrich), 1, 2-hexanediol (90%, Sigma-Aldrich), 3-mercaptopropionic acid (MPA, 99%, Alfa Aesar), tetramethylammonium hydroxide (TMAOH, 98%, Alfa Aesar), platinum(II) acetylacetonate ($\geq 99.98\%$, Sigma Aldrich), methanol ($\geq 99\%$, VWR), toluene ($\geq 99.5\%$, EMD Chemicals), ethanol ($\geq 99\%$, anhydrous, Pharmco), acetone ($\geq 99.5\%$, Sigma-Aldrich), ethyl acetate ($\geq 99\%$, ACROS), hexane (99%, EMD), isopropyl alcohol (IPA $\geq 99.5\%$ Sigma-Aldrich), and potassium hydroxide ($\geq 85\%$, Sigma-Aldrich). All chemicals were used as purchased without further purification.

Synthesis of 1D CdS NRs. 1D CdS NRs were synthesized based on a slightly modified literature reference.⁴⁰ Cadmium and sulfur precursor solutions were first prepared separately. The cadmium precursor solution was prepared by mixing 115 mg (0.45 mmol) CdO, 415 mg (0.75 mmol) TDPA, and 3.5 g TOPO in a 50 mL flask and degassing for 1.5 h at 80 °C. The flask was then heated to 340 °C under Ar flow to form a Cd-TDPA complex indicated by a change in solution color from dark red to optically clear and then cooled to 300 °C. The sulfur precursor solution (S-TOP solution) was prepared by dissolving 110 mg (3.4 mmol) of sulfur powder in 10 mL of degassed TOP.

For a typical synthesis of 1D CdS NRs, 3 mL of the room temperature S-TOP precursor solution was injected into the hot Cd-TDPA solution at 300 °C, and the temperature of the reaction mixture dropped after addition, and then ramped back to 300 °C in ~ 10 min. The remaining S-TOP (~ 7 mL) solution was

injected, 1 mL at a time, every 5 minutes over a 35-minute period, the reaction then proceeded for an additional 30 minutes. At the end of the reaction, the solution was removed from the heating mantle and allowed to cool to approximately 60 °C and then 2-3 mL of chloroform was added to prevent solidification of the crude solution. The CdS NRs were separated from the crude solution by precipitating the particles with ethanol and centrifuging, then dispersed in hexane for optical measurements. The precipitate was further purified once by resuspending the NRs in toluene and then reprecipitating with ethanol and centrifuging.

Synthesis of 1D Mn:CdS NRs. The Mn²⁺ dopant precursor (Mn(S₂CNET₂)) was synthesized by adding 96 mg (0.56 mmol) of NaS₂CNET₂ to a flask and vacuumed to remove air and moisture then refilled with Ar gas. Inside a glovebox, typically, 63 mg (0.2 mmol) of Mn(II) acetate anhydrous and 1 mL of TOP were added to the NaS₂CNET₂ flask. Then the solution was placed under vacuum and heated to 110 °C for further use.

The synthesis of Mn:CdS NRs followed the similar procedure used for CdS NRs except dropwise addition of the 1 mL Mn(S₂CNET₂) precursor into Cd-TDPA solution at 300 °C, before S-TOP injection, and allowed to settle for ~10 minutes. In addition, 9 mL S-TOP (instead of 10 mL S-TOP used in the synthesis of CdS NRs to keep the total volume of the TOP and the reaction the same volume as the undoped CdS NRs) with 2.7 mL of S-TOP is injected first step followed by injecting 0.9 mL every 5 minutes, the reaction then was allowed to proceed for an additional 30 minutes. The same purification method was used as in the undoped CdS NRs.

Synthesis of Pt NP Tipped 1D Mn:CdS-Pt NRs. Pt NP tipped 1D NRs were synthesized based on a slightly modified literature reference.⁴¹ First, OA (0.2 mL), OAm (0.2 mL), and 43.0 mg of 1,2-hexadecanediol (0.17 mmol) were heated in diphenyl ether (9 mL) in a three-neck 25 mL flask at 80 °C under vacuum for 30 min to remove trace amount of water and air. The optical density (OD) of the CdS-based NR stock solution was measured by diluting the stock solution of NRs (100 µL into 1 mL *i.e.*, 100x dilution) and the OD of the NR stock solution can be calculated by the absorbance of the diluted solution multiplied by 100. 65.5 mg (0.17 mmol) Pt(II) acetylacetonate was added to the suspension of the synthesized CdS or Mn:CdS NRs, (Stock Solution OD = 20) in 3 mL of 1, 2-dichlorobenzene and sonicated at 65 °C for 10 min to promote dissolution of the Pt precursor. The reaction mixture was purged with Ar and heated to 200 °C before injecting the 3 mL suspension of Pt precursor and NRs. Typically, after 10 minutes the reaction was removed from heat and quenched in a water bath. The product was washed by precipitation in ethanol followed by centrifugation. The precipitate was further purified twice by resuspending the NRs in hexane and then reprecipitating with ethanol and centrifuging before ligand exchange.

Ligand Exchange. To make water soluble NRs, MPA ligand exchange was performed. Excess amount of MPA (1 mL) was

dissolved in 5 mL methanol and the pH of the solution was adjusted to above 12 with TMAOH. The as-synthesized NRs (typically 0.23 mmol) were dispersed in 5 mL hexane and added to the above 5 mL MPA ligand solution in methanol. The solution was stirred overnight in aluminum foil wrapped containers. The MPA capped NRs were precipitated with ethyl acetate and isolated by centrifugation. The precipitate was further purified once by resuspending the NRs in methanol and then reprecipitating with ethyl acetate and centrifuging.

Sample Characterization. Powder X-ray diffraction (XRD) patterns were taken on a Bruker D2 Phaser with a LYKXEYE 1D silicon strip detector using Cu K α radiation ($\lambda = 1.5406 \text{ \AA}$). Transmission electron microscopy (TEM) images and high-resolution (HR) TEM images were obtained on a JEM 2100F TEM (operated at an accelerating voltage of 200 kV). UV-Visible (UV-Vis) absorption measurements were collected on an Agilent Cary 60 spectrophotometer. The photoluminescence (PL) measurements were performed with a Horiba FluoroMax Plus spectrofluorometer. Time-resolved emission measurements were conducted using an Edinburgh FLS-980 spectrometer with a photomultiplier tube (PMT, R928 Hamamatsu) detector. For CdS NR bandgap PL lifetime measurements, the pulsed excitation light was generated by an Edinburgh EPL-365 pulsed laser diode using at a repetition rate of 0.2 MHz. For Mn²⁺ emission lifetime measurements, the pulsed excitation light was generated by an µF2 60 W xenon flashlamp operating at a repetition rate of 20 Hz. Elemental composition analysis was performed on a PerkinElmer Avio 220 Max inductively coupled plasma-optical emission Spectrometer (ICP-OES). X-ray photoelectron spectroscopy (XPS) analysis was performed using a Thermo Scientific KAlpha+ instrument operating on an Al K α radiation (1486.6 eV). All XPS spectra were calibrated by using the carbon 1s peak at 284.8 eV. Room-temperature X-band EPR spectra were recorded on a Bruker ELEXSYSII E500 spectrometer at a microwave frequency of 9.8 GHz. For cyclic voltammetry (CV), electrochemical impedance spectra (EIS), and photocurrent measurements, a Gamry Interface 1010E electrochemical workstation was used, and the measurements were performed in a single three-electrode setup with the sample electrode as the working electrode, platinum wire as the counter electrode, and Ag/AgCl (0.1 M NaClO₄, E_{Ag/AgCl} = +0.194 V vs. NHE) as the reference electrode. EIS were measured in 0.1 M NaClO₄ at 1.0 V vs NHE with an amplitude of 25 mV (frequency: 100 mHz–100 kHz). The electrochemical electrolyte was degassed for 30 min by flushing with high purity argon prior to CV and EIS measurement. Photocurrent tests were measured in 0.1 M NaClO₄ at 0.3 V vs NHE with a 405 LED light source.

Photocatalytic Water Splitting for Generating Hydrogen Gas. 250 µL (0.009 mg) MPA-ligand exchanged NRs in distilled water (Stock Solution OD = 26) were added to a 15 mL glass centrifuge tube with a stir bar and 2.25 mL distilled water. To each reaction tube, 500 µL of 0.1 M KOH was added to adjust the pH ≥ 12 and 2.5 mL of isopropyl alcohol was added as a sacrificial hole scavenger. The sample solutions were then vacuumed and refilled with Ar gas. The photochemical reactions

were performed in a photochemical reactor equipped with 405 nm LEDs ($\lambda_{\max} = 405 \pm 15$ nm) under stirring at 1000 rpm. The volume of the generated H_2 gas was collected in a burette and recorded every 15 or 30 minutes.

RESULTS

1D Mn:CdS-Pt NRs. In this study, we synthesized Mn^{2+} doped 1D CdS NRs with Pt NP tips (*i.e.*, Mn:CdS-Pt NRs) to study the role of dopants and metal co-catalyst on the photocatalytic performance. Firstly, 1D Mn:CdS NRs were synthesized via a hot-injection method by injecting S-precursor into Cd and Mn-precursor in trioctylphosphine/trioctylphosphine oxide (TOP/TOPO) solution at 300 °C. The undoped CdS NRs were also synthesized for comparison with the same procedure without adding the Mn-precursor in the reaction. The as-obtained Mn:CdS NRs were then tipped with Pt by reduction of Pt in diphenyl ether with 1,2 hexadecanediol at 200 °C (See details in the Experimental Section).

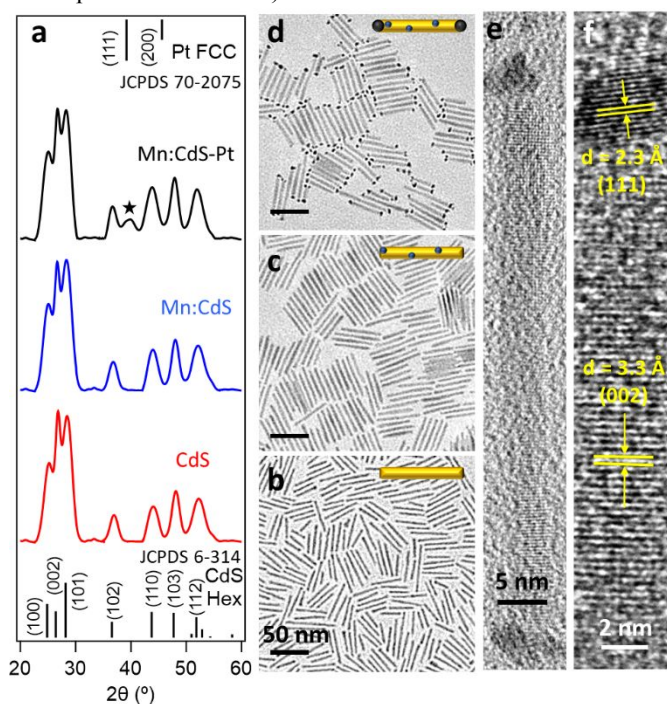


Fig 2. a) The powder XRD patterns of 1D CdS, Mn:CdS, and Mn:CdS-Pt CdS-based NRs (★ indicates the diffraction peak from Pt). TEM images of (b) CdS NRs, (c) Mn:CdS NRs, and (d) Mn:CdS-Pt NRs; HR-TEM images of (e) a Mn:CdS-Pt NR and (f) a portion of a Mn:CdS-Pt NR showing the d spacing of 3.3 Å and 2.3 Å of the (002) plane of the CdS NR and (111) plane of the Pt NP tip, respectively.

The structure and morphology of the 1D CdS NR-based photocatalysts were characterized by X-ray diffraction (XRD) and transmission electron microscopy (TEM). The XRD patterns of the undoped and Mn^{2+} doped CdS NRs, as well as the Mn:CdS-Pt NRs indicate hexagonal phase CdS in these 1D NRs (Figure 2a).^{42, 43} Compared with the standard hexagonal CdS XRD pattern, the (002) diffraction peak is obviously intensified,

indicating the cylindric growth for non-spherical NCs along the [001] direction (perpendicular to the (002) plane). TEM images (Figure 2b-c) of the as-synthesized products show both CdS and Mn:CdS to be 1D cylindrical NRs with an average diameter of 4.1 ± 0.3 nm and 4.2 ± 0.3 nm, and an average length of 52 ± 5 nm and 50 ± 5 nm, respectively. The TEM images and histogram analysis (Figure S1a-d) show no significant difference in the diameter and length of the 1D NRs despite the addition of Mn^{2+} dopants. After adding Pt at the tips of Mn:CdS NRs, a new XRD peak is present at 39.7° , which can be assigned as the (111) plane of Pt (indicated as the ★ in Figure 2a).⁴¹ The TEM image of the Mn:CdS-Pt NRs indicates small, dark Pt NPs with an average diameter of 4.4 ± 0.5 nm tipped at both ends of the CdS NRs with a “dumbbell” type shape (Figure 2d). The average diameter of Mn:CdS in Mn:CdS-Pt NRs is 4.1 ± 0.3 nm and the average total length, including the Pt tips, is 58 ± 5 nm (Figure S1e-f). The slightly longer Mn:CdS-Pt NRs, compared to the NRs without the Pt tips, are consistent with the addition of the two Pt NPs on each end of the NRs (Figure S1f and S1g). The HR-TEM image of Mn:CdS-Pt NRs (Figure 2e and 2f) shows a lattice fringe of 3.3 Å from the (002) plane of hexagonal CdS NRs and a lattice fringe of 2.3 Å from the (111) plane of a face-centered cubic (fcc) Pt lattice (Figure 2f).

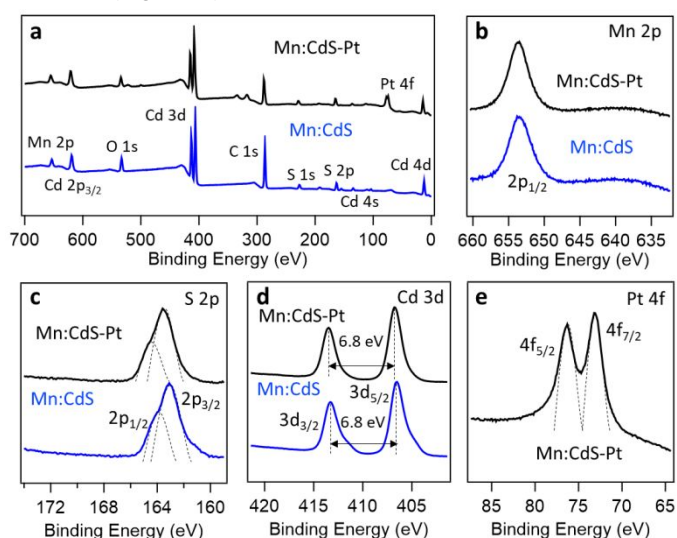


Fig 3. X-ray photoelectron spectroscopy (XPS) of 1D Mn:CdS, and Mn:CdS-Pt NRs, where a) is the survey spectrum, and the spectra of b) the Mn 2p orbitals, c) the S 2p orbitals, d) the Cd 3d orbitals, and e) the Pt 4f orbitals.

The survey XPS spectrum (Figure 3a) of the Mn:CdS NRs shows distinct peaks for Cd 3d, S 2s, and Mn 2p. For the untipped Mn:CdS NRs, the Mn^{2+} dopant peak is at 653.5 eV ($2p_{1/2}$) (Figure 3b), the S 2p peaks are at 163.1 eV ($2p_{3/2}$) and 164 eV ($2p_{1/2}$) (Figure 3c), and the Cd 3d peaks are at 406.5 eV ($3d_{5/2}$) and 413.3 eV ($3d_{3/2}$) (Figure 3d), which is consistent with the literature reported values.^{44,45} For the Mn:CdS-Pt NRs, similar peaks were observed for Mn, Cd, and S with a new peak present for Pt 4f at 73.2 eV ($4f_{7/2}$) and 76.3 eV ($4f_{5/2}$) which are also consistent with literature reported values.⁴⁶ The Mn, Cd, and S peaks exhibit a small peak shift towards the higher binding

energy (0.2 eV for Mn 2p_{1/2}, 0.3 eV for Cd 3d_{5/2} and 3d_{3/2}, and 0.5 eV for S 2p_{3/2}) in the XPS spectra when comparing the Mn:CdS NRs, which indicates that the electrons in both the CdS host CB and the Mn²⁺ dopant energy level are interacting with the Fermi level of Pt. In addition, the distance between the Cd 3d_{5/2} and Cd 3d_{3/2} peaks stays consistent at 6.8 eV, so the shift of the peak position is due to Fermi level equilibration occurring as electrons transfer from the Mn:CdS NRs to Pt.^{47, 48}

Optical Properties. The absorption and photoluminescence (PL) spectra for the 1D CdS, Mn:CdS, and Mn:CdS-Pt NRs (Figure 4a) show the first exciton absorption peak at ~470 nm, from CdS, for all NRs. For CdS and Mn:CdS NRs, the CdS bandgap PL is at 480 nm and has a broad defect emission peak centered around ~650 nm, with PL quantum yields (QYs) of 7.4% and 6.7%, respectively. There is no clear Mn²⁺ emission (usually around 600 nm) present in the Mn:CdS NRs, which might be due to the large amount of surface trapping states considering the large surface to volume ratio of 1D NRs.⁴⁹ However, the Mn²⁺ PL peak at 600 nm can be observed after ZnS surface passivation (*i.e.*, 1D Mn:CdS/ZnS NRs) to remove the surface defects (Figure S2). The wider bandgap ZnS shell was chosen to form CdS/ZnS type I core/shell NRs to completely confine the electrons and holes within the CdS core, and therefore the PL spectra is not sensitive to surface defects of NRs (See detailed energy levels of dopants and surface defects, and band alignment of type I CdS/ZnS structure in Figure S3).^{39, 49-52} Furthermore, despite the lack of obvious Mn²⁺ emission, ICP-OES measurements indicate 0.9% Mn²⁺ dopant concentration in the Mn:CdS NRs, which correspond with ~110 Mn²⁺ ions per NR. Upon the addition of Pt to the tips of the NRs, a loss of most of the emission features was observed and the PL QY decreases to 0.9% due to the charge transfer from Mn:CdS NRs to metal Pt NP tips (Figure 4a).

The calculated lifetimes for the CdS PL of the NRs are shown in Figure 4b with 7.9 ns for CdS, 3.8 ns for Mn:CdS, and 1.4 ns for Mn:CdS-Pt NRs (Figure 4b and insert). Compared with CdS NRs, the shorter lifetime of the band edge PL from Mn:CdS NRs can be attributed to the host to Mn²⁺ dopants energy transfer as an added electron relaxation pathway. Further significant decrease in the CdS PL lifetime after the Pt NPs are tipped onto the NRs occurs, which is consistent with the electron transfer from the excited states of Mn:CdS NRs to the Fermi energy level of Pt NPs. To prove the electron transfer from the Mn²⁺ dopants to the Pt NP cocatalyst, the Mn²⁺ emission lifetime of Mn:CdS/ZnS and Pt tipped Mn:CdS/ZnS NRs (*i.e.*, 1D Mn:CdS-Pt/ZnS NRs) was measured. The Mn²⁺ emission lifetime from Mn:CdS/ZnS core/shell NRs was found to be 4.1 ms, which dramatically decreased to 0.29 ms after introducing the Pt NP tips on the Mn:CdS-Pt/ZnS NRs (Figure 4c), indicating the electron transfer from the excited states of Mn²⁺ dopants to the Fermi energy level of Pt NPs. The lifetime of the broad emission at 600 nm for CdS and Mn:CdS NRs without shell passivation was also measured to be 6.9 μs and 7.5 μs, respectively. The slightly longer lifetime of the broad emission in Mn:CdS NRs

might be due to the combination of defect emission (~μs) and Mn²⁺ emission (~ms) (Figure S4).

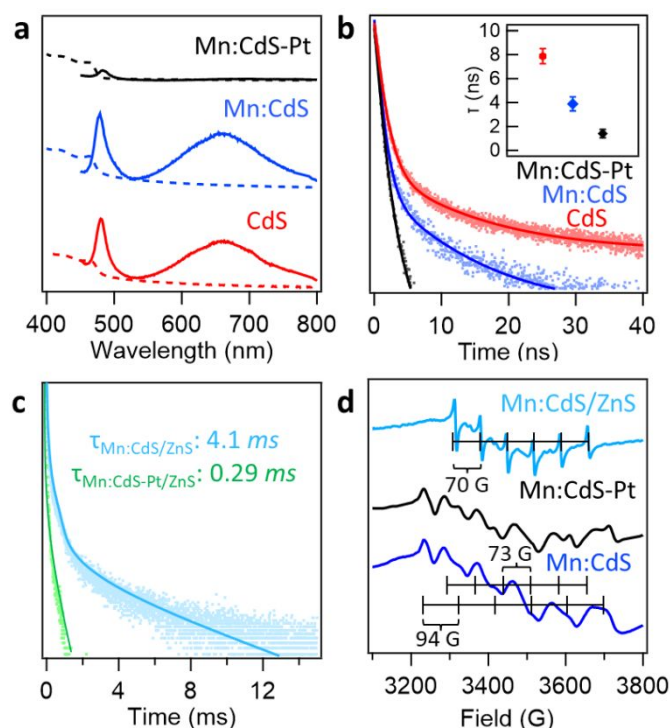


Fig 4. a) Absorbance (dashed lines) and PL spectra (solid lines) of CdS, Mn:CdS, and Mn:CdS-Pt NRs. b) PL decays of the CdS emission for CdS, Mn:CdS, and Mn:CdS-Pt NRs. Inset are the calculated lifetimes (τ) in ns. c) Mn²⁺ lifetime from core/shell Mn:CdS/ZnS and Mn:CdS-Pt/ZnS NRs. d) Room-temperature X-band EPR spectra of Mn:CdS, Mn:CdS-Pt, and Mn:CdS/ZnS NRs.

The presence of Mn²⁺ dopants within the CdS host lattice was further confirmed by X-band EPR spectroscopy (Figure 4d). In the Mn:CdS and Mn:CdS-Pt NRs, there are two sets of six-peak hyperfine splitting patterns with hyperfine constants (A) of 94 and 73 G, corresponding to the Mn²⁺ ions on the surface and the core of the CdS lattice, respectively, indicating random distribution of Mn²⁺ dopants in the CdS NR lattice.^{49, 53, 54} The EPR of the Mn:CdS/ZnS NRs (Figure 4d) only shows a singular hyperfine peak splitting pattern of 70 G from the core Mn²⁺ dopants. The dismissal of the larger EPR hyperfine splitting (94 G) after shell coating further proves the larger and smaller EPR hyperfine splitting patterns (94 and 73 G) from the Mn:CdS NRs are from the surface and core Mn²⁺ dopants, respectively.

Electrochemical Properties. To further confirm the role of the long lifetime Mn²⁺ dopant ions to mediate the efficient electron transport from host CdS NRs to Pt co-catalysts, the charge transport properties of the CdS-based NRs were studied by electrochemical impedance spectroscopy (EIS). The EIS data in the form of a Nyquist plot (Figure 5a) shows that the Mn²⁺ doped CdS NRs have a smaller semicircle arc than that of undoped CdS NRs. The as-calculated values for R_s and R_{ct} for CdS are 128.4 Ω and 5552 Ω, respectively while for Mn:CdS R_s and R_{ct} are 161.1 Ω and 1372 Ω, respectively, which shows the decreased

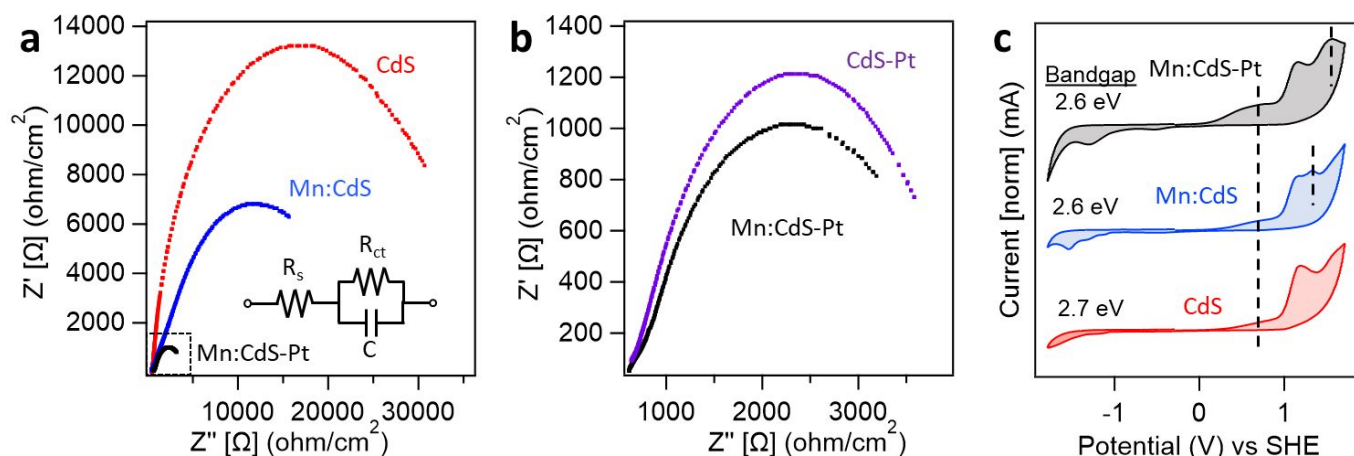


Fig 5. a) Electrochemical impedance spectra (Nyquist plot) of CdS, Mn:CdS, and Mn:CdS-Pt, where Z' and $-Z''$ are the virtual and real impedances, respectively. In the inset circuit diagram, R_s represents the electrolyte resistance, R_{ct} represents the charge transfer resistance, and C represents the capacitance. b) Magnified impedance spectra area (dotted box) of Figure 4a) highlighting the decrease in impedance from CdS-Pt to Mn:CdS-Pt. c) Normalized cyclic voltammetry spectra of CdS, Mn:CdS, and Mn:CdS-Pt NRs.

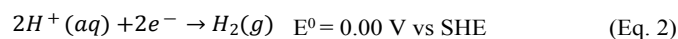
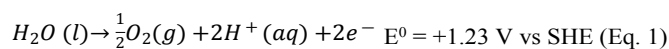
charge transfer resistance for the CdS-based NRs upon the addition of Mn^{2+} dopants. Further dramatic reduction of charge transport resistance was obtained by Pt tipping in the Mn:CdS-Pt NRs with an extremely small semicircle arc with R_s and R_{ct} calculated as 80.2Ω and 499.9Ω , respectively.

To confirm the role of the long lifetime dopant ions for the low charge transport resistance due to the facilitated electron transport from host semiconductor NRs to Pt NP co-catalysts, we synthesized the CdS NRs with Pt tips but without Mn^{2+} dopant incorporation (*i.e.*, CdS-Pt NRs) in a control experiment (See SI for the synthesis and characterization of CdS-Pt NRs). The CdS-Pt NRs have roughly the same diameter and length as the Mn:CdS-Pt NRs based on XRD and TEM analysis (Figure S5a-b), analogous to the CdS and Mn:CdS NRs. Compared with the EIS spectra of the CdS-Pt NRs where the calculated R_s and R_{ct} values are 92.6Ω and 508.6Ω , the Mn:CdS-Pt NRs have a smaller semicircle arc (Figure 5b and S7a) and a lower R_{ct} , which confirms that further facilitated electron transfer from Mn^{2+} dopants to Pt NPs can be achieved. In addition, the band edge emission lifetime for Mn:CdS-Pt NRs is shorter than the CdS-Pt NRs (Figure 3b and S6b), showing facilitated electron transfer upon the addition of Mn^{2+} dopants with longer PL lifetime in Mn:CdS-Pt NRs. To further confirm the enhanced electron-hole separation and charge transport in the Mn:CdS-Pt NRs, photocurrent tests were performed for the CdS-based NRs (Figure S8). The transient photocurrent responses increased after the incorporation of Mn^{2+} dopants in the CdS NRs, and further significant photocurrent enhancement was achieved after adding Pt NP tips on the Mn:CdS NRs, which is consistent with the reduced charge transport resistance in Mn:CdS-Pt NRs from EIS data (Figure 5a and 5b).

Cyclic voltammetry (CV) was used to study the bandgap and thus the suitability of the 1D CdS NR-based photocatalysts for catalytic water reduction (Figure 5c and S7b). The position of the oxidative band (*i.e.*, conduction band) can be measured by finding the onset of the current increase during the increase of

the potential on the CV which occurs at ~ 0.8 V vs SHE (Figure 5c and S7b). Based on the bandgap calculated in a Tauc Plot from the absorbance data, the position of the valence band can be obtained (Table S1), the CdS-based NRs show a bandgap of ~ 2.6 eV.

For photocatalytic H_2 generation by the reduction of water (gaining electrons), the half reactions and reduction potentials are shown below in equations 1 and 2.



The bandgaps of each NR set-up (Figure 5c and S7b) are wide enough to cover the 1.23 eV needed to split water. For the Mn^{2+} doped NRs, there is an increase in the area under the CV curve at ~ 0.8 V and an added peak at ~ 1.3 V and ~ 1.5 V for Mn:CdS and Mn:CdS-Pt, respectively. This could be attributed to the presence of the Mn^{2+} dopants as the CV measures the available states for electrons to be added. In the presence of Pt tips, the peak at ~ 1.3 V has a slight shift to ~ 1.5 V which could be due to the movement of the electrons to the available Fermi level of Pt.

Photocatalytic H_2 Generation by Water Splitting.

Photocatalytic water splitting experiments were conducted with the as synthesized NRs under blue light (405 nm LED) irradiation. Figure 6a shows the catalytic performance of the 1D CdS NR-based NRs. The CdS NRs generated 120 mmol of hydrogen gas over 8 hours (9.4 mmol/hour/g) with an internal quantum efficiency (IQE) of 0.5% (See SI for the calculation of IQE). Mn:CdS NRs generated 149 mmol of hydrogen gas over the same period (19.8 mmol/hour/g) with a greater IQE of 1.0% (Figure S9). A plausible reason for the increase in the photocatalytic yields from undoped NRs to the Mn^{2+} doped NRs comes from the host-to-dopant energy transfer in the Mn:CdS NRs, which provides excited electrons with longer lifetimes, and therefore are more accessible to take part in the photocatalytic

reduction reactions. The higher photocatalytic performance of Mn:CdS NRs than CdS NRs is also consistent with the smaller charge transport resistance of Mn:CdS NRs from EIS measurements (Figure 5b).

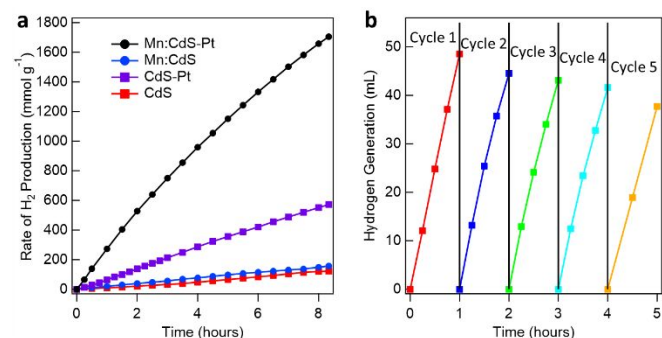


Fig 6. a) Photocatalytic performance of the 1D CdS, CdS-Pt, Mn:CdS, and Mn:CdS-Pt. b) Recycle test for the Mn:CdS-Pt photocatalytic system.

Upon the addition of Pt tips, the 1D Mn:CdS-Pt NRs show an excellent overall hydrogen generation with 1658 mmol of H₂ gas generated per gram of photocatalyst over 8 hours (287 mmol/hour/g), with an IQE of 13.8% (Figure S9). The enhanced charge separation is due to the synergistic effect between long lifetime Mn²⁺ dopants and following electron transfer to the Fermi level of Pt (\sim ps); electrons accumulate in the Pt NP tips for subsequent photoreduction reactions with an impressive increase in overall photocatalytic performance. The dramatically increased lifetimes of the Mn²⁺ dopants (\sim ms) compared to the fast exciton relaxation (\sim ns) of the undoped CdS NR facilitates the likelihood of the excited electron to move to the Pt NPs for photocatalysis.

Recycle tests were also performed to study the stability of the photocatalysts, in which the photocatalyst was re-collected and the photocatalytic solution was remade by adding the same amount of hole scavenger at the same pH (Figure 6b). The hour-by-hour recycling reaction using 1D Mn:CdS-Pt photocatalyst revealed that a stable \sim 94% performance of the previous photocatalytic result, and the photocatalytic efficiency was maintained at \sim 78% of the initial performance after five consecutive cycles. The \sim 6% cycle-by-cycle loss could be attributed to the wash/cleaning loss of the samples as well as possible partial photodegradation⁵⁵ of the 1D Mn:CdS-Pt NRs.

To verify the sources of sample losses, ICP-OES analysis was performed to measure the concentration of Cd in the supernatant of the photocatalytic solution during the centrifugation step between cycles. The trace amount of Cd in the supernatant should be due to the wash losses of the NRs since it is impossible to recollect all NRs from centrifugation, as well as due to possible photodegradation during photocatalytic reactions. The [Cd] from collected supernatants after each cycle test is shown in Table S2, which indicates on average \sim 4.1% sample loss for each cycle. In addition, the transfer of the NRs to and from the glass tube could also lead to the loss of trace amount of NR

sample (See detailed discussion in Supporting Information). Therefore, the sample losses from wash, transfer, and photodegradation contribute to the slight decrease of photocatalytic performance of H₂ generation per cycle.

Furthermore, the recycle test was also performed over 30-hour period in 10-hour cycles to assess the long-term stability of the system (Figure S10). The cycle-by-cycle photocatalytic yields were 93% and 83% in the second and third 10-hour cycles, respectively, indicating good reusability of the 1D photocatalysts.

DISCUSSION

Photocatalytic Mechanism of the 1D Mn:CdS-Pt NRs. Figure 7a illustrates the host-to-dopant energy transfer and following electron transport to the Fermi level of Pt co-catalyst in the 1D Mn:CdS-Pt NR-based photocatalysts for H₂ gas generation. The interactions between the long lifetime Mn²⁺ dopants and the Pt NP co-catalyst highlights the critical two-step charge carrier transport, *i.e.*, 1) host-to-dopant energy transfer followed by 2) electron transfer to Pt NPs, which can help prevent the fast exciton recombination (\sim ns) and maintain the charge separated states.

The shorter CdS PL lifetime of the Mn:CdS NRs compared to that of pristine CdS NRs (Figure 4b) indicates the host-to-dopant energy transfer (Step 1). The following electron transfer (Step 2) from Mn:CdS to Pt is demonstrated by the decrease in PL QY after Pt NP tipping (from 6.7% to 0.9%, Figure 4a). In addition, the Mn²⁺ dopant PL lifetime in the Mn:CdS/ZnS type I core/shell NRs also decreases after adding Pt tips due to electron transfer from Mn²⁺ dopants to Pt NP tips (Figure 4c). Further evidence of the two successive steps is demonstrated by the reduced charge transport resistance and enhanced charge transport from CdS to Mn:CdS to Mn:CdS-Pt NRs by EIS data (Figure 5a and 5b) and photocurrent result (Figure S8), respectively. The longer lifetime Mn²⁺ dopants can function as a bridge between the light harvesting CdS and active catalytic Pt NPs with lower potential Fermi level (by dopant to Pt electron transfer) for enhanced charge transport, which leads to a greater water splitting efficiency.

Mn²⁺ Dopant Concentration-Dependent Photocatalytic Performance. To further confirm the critical role of Mn²⁺ dopants in the Mn:CdS-Pt NRs, a control experiment of photocatalytic water splitting using undoped CdS-Pt NRs was also performed. However, the CdS-Pt NRs generated 551 mmol of H₂ gas per gram of photocatalyst over 8 hours (64 mmol/hour/g) (Figure 6a) and had an IQE of 3.1%, which is only 22.2% of the yield of Mn:CdS-Pt NRs (Figure 6b). In this study, an optimal Mn²⁺ dopant concentration was identified as 0.9% in the as synthesized CdS NRs.

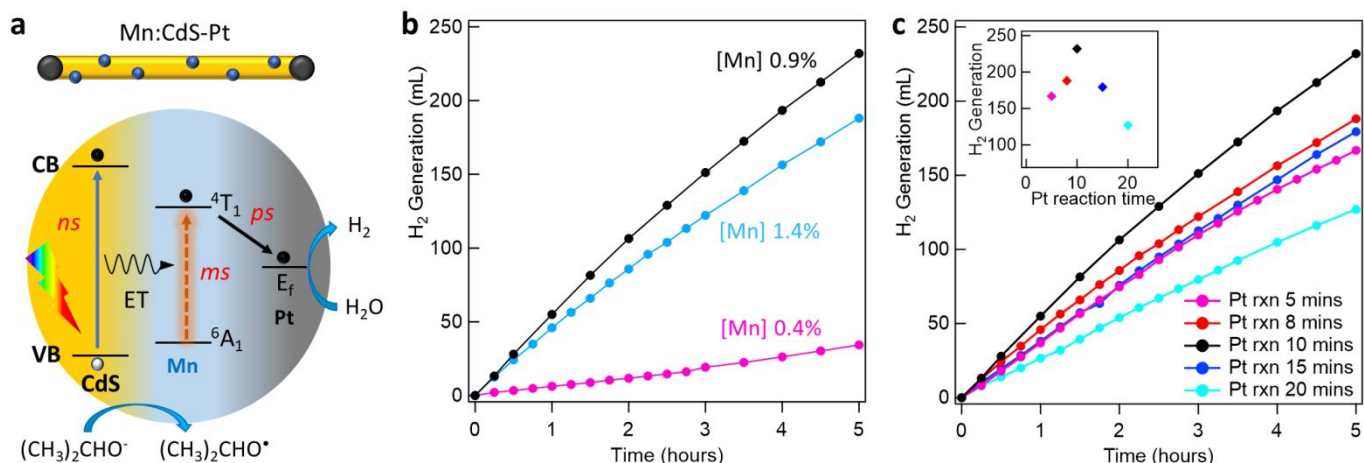


Fig 7. a) Schematic representation of the host-to-dopant energy transfer and following electron transport to the Fermi level of Pt co-catalyst in the 1D Mn:CdS-Pt NR-based photocatalysts for H₂ gas generation by water splitting. b) Photocatalytic performance of the Mn:CdS-Pt NRs with differing Mn²⁺ doping concentrations. c) Pt reaction photocatalysis yields for 5 to 20 minutes of Pt tipping reaction time.

At higher Mn²⁺ concentrations (1.4%), the photocatalytic yield fell to 81% of the ideal Mn:CdS-Pt NRs (Figure 7b), which is due to short-range Mn-Mn interactions, leading to a concentration quenching effect as shown by a broad dipolar EPR peak without the well-resolved hyperfine peaks (Figure S11c). Concentration dependent quenching is common at higher doping concentrations due to the cross-relaxation between Mn-Mn coupled dopants where the dopants are closer to each other.^{56, 57} The concentration quenching effect can also be seen in the PL lifetime spectra of the Mn²⁺ doped NRs as the Mn²⁺ PL lifetime decreases from 4.1 to 2.9 ms when the Mn²⁺ concentration increases from 0.9% to 1.4% of the corresponding Mn:CdS/ZnS NRs (Figure S11b and inset). In addition, the CdS band edge PL lifetime also decreases from 3.8 to 1.4 ns as there are more Mn²⁺ ions providing an alternative relaxation pathway (Figure S11a and inset).

At lower Mn²⁺ concentrations, there are fewer energy transfer acceptors in the host-to-dopant energy transfer system in the Mn:CdS NRs. The lifetime of the Mn²⁺ PL lifetime stays relative constant from 4.1 to 4.0 ms when the Mn²⁺ concentration decreases from 0.9% to 0.4% of the corresponding Mn:CdS/ZnS NRs (Figure S11b and inset). However, with limited Mn²⁺ dopants available at 0.4% Mn²⁺ doping concentration, fewer excited excitons can transfer their energy to Mn²⁺ dopants, and therefore, the photocatalytic yield fell to 15% of the ideal Mn:CdS-Pt NRs (Figure 7b). This reduced host-to-dopant energy transfer at low doping concentration can be seen in the PL lifetime spectra where the band edge PL lifetime increases from 3.8 to 6.5 ns when the Mn²⁺ concentration decreases from 0.9% to 0.4% (Figure S11a and inset).

Size and Number of Pt Tip(s)-Dependent Photocatalytic Performance. Previous work has shown that 1D NRs tipped on both ends showing an increase in their hydrogen reduction yields compared to 1D NRs tipped at only one end.⁵⁸ The Pt co-catalyst on each end of the NR allows more electrons to transfer to Pt NPs and also creates active sites on both Pt tips upon which

hydrogen can adsorb onto. Once the electrons have moved to Pt, they are less likely to leave the Pt NPs and recombine within CdS as the Pt has a higher work function than that of the semiconductor CdS.¹⁷ Therefore, the bridging effect from long lifetime Mn²⁺ dopant ions is amplified in the presence of Pt (Figure 7a) as indicated by the decreased PL QYs (Figure 3a) and electrochemical impedance (Figure 5a).

To control the size and number of Pt tips on 1D NRs, the Pt reaction time-dependent experiments were performed. In general, the longer the Pt tipping reaction goes, the more likely there will be larger Pt tips as well as Pt co-catalysts forming on both ends of the NRs while shorter Pt reaction times lead to smaller Pt tips and on only one end. In a typical 10 min Pt tipping reaction, dumbbell shaped Mn:CdS-Pt NR with Pt tipped on each end of the NRs were obtained. When the Pt reaction time was reduced to 5 minutes, the smaller Pt NPs with the average diameter of 3.2 ± 0.3 nm (Figure S12b) were obtained and often only tipped on one end of the NRs (Figure S12a). The lack of a dumbbell type NR led to lower photocatalytic performance of H₂ generation with 72% of the ideal Mn:CdS-Pt NRs (Figure 7c inset).

When the Pt reaction time was increased to 15 min and above, increased Pt NP size (5.4 ± 0.4 nm under 15 min reaction, Figure S12 c-d) was obtained. However, greater light scattering and absorption by the Pt co-catalyst (instead of CdS NRs) occurred which lowered the light harvesting ability of the Mn:CdS NRs and consequently, the photocatalytic performance of the NRs with Pt tipping reaction time of 15 min was reduced to 90% of the ideal Mn:CdS-Pt NRs. Further increase of Pt tipping reaction time results in a more dramatic decrease in the H₂ generation efficiency (Figure 7c and inset). Therefore, the 1D Mn:CdS NRs with Pt tips on both ends with similar diameter of the NRs are ideal for efficient light harvesting and corresponding photocatalytic water splitting.

CONCLUSIONS

We have developed a new functional Mn²⁺ doped 1D CdS NRs tipped with Pt NPs (*i.e.*, Mn:CdS-Pt NRs) for photocatalytic water splitting. The energy transfer from 1D CdS host NRs to a long lifetime bridging Mn²⁺ ions followed by electron transfer to the hydrophilic Pt tips of the Mn:CdS-Pt NRs limits the fast charge recombination in the host CdS NRs, which leads to highly efficient photocatalysts for H₂ generation. EIS analysis indicates lower charge transport resistance after the incorporation Mn²⁺ dopants with long lifetimes (\sim ms) inside CdS NRs due to the host-to-dopant energy transfer. Further significant decrease of impedance after the tipped with Pt NPs occurs as the result of electron transfer from the NRs to the metal NPs. Our rationally designed 1D Mn:CdS-Pt NR photocatalysts take advantage of the long lifetime of Mn²⁺ dopants (\sim ms) for efficient charge separation and electron transfer, exhibiting \sim 4.5 times greater photocatalytic yields of H₂ generation from water splitting than undoped CdS-Pt NRs. The functional 1D photocatalysts by introducing dopants as charge transport bridges provides new opportunities for facilitated electron transfer of high performance photocatalysts.

AUTHOR CONTRIBUTIONS

Corresponding Author

*Weiwei Zheng - Department of Chemistry, Syracuse University, Syracuse, New York 13244, United States; <http://orcid.org/0000-0003-1394-1806>; Email: wzhen104@syr.edu

Conflicts of interest

There are no conflicts to declare.

ACKNOWLEDGEMENTS

W.Z. acknowledges support from NSF CAREER (CHE-1944978) and NSF IUCRC Phase I grant (2052611). We thank A. Guinness and A. Beaton Jr for their aid with EPR measurements. We also thank B. Zink for his insights and help with TEM measurements.

REFERENCES

1. Edwards, P. P.; Kuznetsov, V. L.; David, W. I. Hydrogen energy. *Philos Trans A Math Phys Eng Sci* 2007, **365**, (1853), 1043-56.
2. Wu, K.; Lian, T. Quantum confined colloidal nanorod heterostructures for solar-to-fuel conversion. *Chem. Soc. Rev.* 2016, **45**, (14), 3781-3810.
3. Yu, J.; Yu, Y.; Zhou, P.; Xiao, W.; Cheng, B. Morphology-dependent photocatalytic H₂-production activity of CdS. *Appl. Catal., B* 2014, **156-157**, 184-191.
4. Kim, K.; Kim, M.-J.; Kim, S.-I.; Jang, J.-H. Towards Visible Light Hydrogen Generation: Quantum Dot-Sensitization via Efficient Light Harvesting of Hybrid-TiO₂. *Sci. Rep.* 2013, **3**, (1), 3330.
5. Li, Z.-J.; Fan, X.-B.; Li, X.-B.; Li, J.-X.; Zhan, F.; Tao, Y.; Zhang, X.; Kong, Q.-Y.; Zhao, N.-J.; Zhang, J.-P.; Ye, C.; Gao, Y.-J.; Wang, X.-Z.; Meng, Q.-Y.; Feng, K.; Chen, B.; Tung, C.-H.; Wu, L.-Z. Direct synthesis of all-inorganic heterostructured CdSe/CdS QDs in aqueous solution for improved photocatalytic hydrogen generation. *J. Mater. Chem. A* 2017, **5**, (21), 10365-10373.
6. Li, Z.-J.; Wang, J.-J.; Li, X.-B.; Fan, X.-B.; Meng, Q.-Y.; Feng, K.; Chen, B.; Tung, C.-H.; Wu, L.-Z. An Exceptional Artificial Photocatalyst, Ni_h-CdSe/CdS Core/Shell Hybrid, Made In Situ from CdSe Quantum Dots and Nickel Salts for Efficient Hydrogen Evolution. *Adv. Mater.* 2013, **25**, (45), 6613-6618.
7. Trevisan, R.; Rodenas, P.; Gonzalez-Pedro, V.; Sima, C.; Sanchez, R. S.; Barea, E. M.; Mora-Sero, I.; Fabregat-Santiago, F.; Gimenez, S. Harnessing Infrared Photons for Photoelectrochemical Hydrogen Generation. A PbS Quantum Dot Based "Quasi-Artificial Leaf". *J. Phys. Chem. Lett.* 2013, **4**, (1), 141-146.
8. Yu, L.; Chen, W.; Li, D.; Wang, J.; Shao, Y.; He, M.; Wang, P.; Zheng, X. Inhibition of photocorrosion and photoactivity enhancement for ZnO via specific hollow ZnO core/ZnS shell structure. *Appl. Catal., B* 2015, **164**, 453-461.
9. Meng, A.; Zhu, B.; Zhong, B.; Zhang, L.; Cheng, B. Direct Z-scheme TiO₂/CdS hierarchical photocatalyst for enhanced photocatalytic H₂-production activity. *Appl. Surf. Sci.* 2017, **422**, 518-527.
10. Yuan, J.; Wen, J.; Gao, Q.; Chen, S.; Li, J.; Li, X.; Fang, Y. Amorphous Co₃O₄ modified CdS nanorods with enhanced visible-light photocatalytic H₂-production activity. *Dalton Trans.* 2015, **44**, (4), 1680-1689.
11. Nasir, J. A.; Rehman, Z. u.; Shah, S. N. A.; Khan, A.; Butler, I. S.; Catlow, C. R. A. Recent developments and perspectives in CdS-based photocatalysts for water splitting. *J. Mater. Chem. A* 2020, **8**, (40), 20752-20780.
12. Wu, K.; Chen, Z.; Lv, H.; Zhu, H.; Hill, C. L.; Lian, T. Hole removal rate limits photodriven H₂ generation efficiency in CdS-Pt and CdSe/CdS-Pt semiconductor nanorod-metal tip heterostructures. *J Am Chem Soc* 2014, **136**, (21), 7708-16.
13. Corby, S.; Rao, R. R.; Steier, L.; Durrant, J. R. The kinetics of metal oxide photoanodes from charge generation to catalysis. *Nat. Rev. Mater.* 2021, **6**, (12), 1136-1155.
14. Wang, J.; Xiong, L.; Bai, Y.; Chen, Z.; Zheng, Q.; Shi, Y.; Zhang, C.; Jiang, G.; Li, Z. Mn-Doped Perovskite Nanocrystals for Photocatalytic CO₂ Reduction: Insight into the Role of the Charge Carriers with Prolonged Lifetime. *Sol. RRL* 2022, **6**, (8), 2200294.
15. Ge, L.; Zuo, F.; Liu, J.; Ma, Q.; Wang, C.; Sun, D.; Bartels, L.; Feng, P. Synthesis and Efficient Visible Light Photocatalytic Hydrogen Evolution of Polymeric g-C₃N₄ Coupled with CdS Quantum Dots. *J. Phys. Chem. C* 2012, **116**, (25), 13708-13714.
16. Jang, J. S.; Joshi, U. A.; Lee, J. S. Solvothermal Synthesis of CdS Nanowires for Photocatalytic Hydrogen and Electricity Production. *J. Phys. Chem. C* 2007, **111**, (35), 13280-13287.
17. Li, Q.; Zhao, F.; Qu, C.; Shang, Q.; Xu, Z.; Yu, L.; McBride, J. R.; Lian, T. Two-Dimensional Morphology Enhances Light-Driven H₂ Generation Efficiency in CdS Nanoplatelet-Pt Heterostructures. *J. Am. Chem. Soc.* 2018, **140**, (37), 11726-11734.
18. Muruganandham, M.; Kusumoto, Y.; Okamoto, C.; Muruganandham, A.; Abdulla-Al-Mamun, M.; Ahmmad, B. Mineralizer-Assisted Shape-Controlled Synthesis, Characterization, and Photocatalytic Evaluation of CdS Microcrystals. *J. Phys. Chem. C* 2009, **113**, (45), 19506-19517.
19. Bao, N.; Shen, L.; Takata, T.; Domen, K. Self-Templated Synthesis of Nanoporous CdS Nanostructures for Highly Efficient Photocatalytic Hydrogen Production under Visible Light. *Chem. Mater.* 2008, **20**, (1), 110-117.

20. Diroll, B. T.; Koschitzky, A.; Murray, C. B. Tunable Optical Anisotropy of Seeded CdSe/CdS Nanorods. *J. Phys. Chem. Lett.* 2014, **5**, (1), 85-91.
21. Liu, Y.; Yang, W.; Chen, Q.; Cullen, D. A.; Xie, Z.; Lian, T. Pt Particle Size Affects Both the Charge Separation and Water Reduction Efficiencies of CdS–Pt Nanorod Photocatalysts for Light Driven H₂ Generation. *J. Am. Chem. Soc.* 2022, **144**, (6), 2705-2715.
22. Wu, K.; Zhu, H.; Lian, T. Ultrafast exciton dynamics and light-driven H₂ evolution in colloidal semiconductor nanorods and Pt-tipped nanorods. *Acc. Chem. Res.* 2015, **48**, (3), 851-9.
23. Berr, M.; Vaneski, A.; Susha, A. S.; Rodríguez-Fernández, J.; Döblinger, M.; Jäckel, F.; Rogach, A. L.; Feldmann, J. Colloidal CdS nanorods decorated with subnanometer sized Pt clusters for photocatalytic hydrogen generation. *Appl. Phys. Lett.* 2010, **97**, (9), 093108.
24. Chen, K.; Ding, S.-J.; Ma, S.; Wang, W.; Liang, S.; Zhou, L.; Wang, Q.-Q. Enhancing Photocatalytic Activity of Au-Capped CdS–PbS Hetero-octahedrons by Morphology Control. *J. Phys. Chem. C* 2020, **124**, (14), 7938-7945.
25. Hao, J.; Liu, H.; Wang, K.; Sun, X. W.; Delville, J.-P.; Delville, M.-H. Hole Scavenging and Electron–Hole Pair Photoproduction Rate: Two Mandatory Key Factors to Control Single-Tip Au–CdSe/CdS Nanoheterodimers. *ACS Nano* 2021, **15**, (9), 15328-15341.
26. Wang, H.; Chen, W.; Zhang, J.; Huang, C.; Mao, L. Nickel nanoparticles modified CdS – A potential photocatalyst for hydrogen production through water splitting under visible light irradiation. *Int. J. Hydrogen Energy* 2015, **40**, (1), 340-345.
27. Zhang, B.; Chen, C.; Liu, J.; Qiao, W.; Zhao, J.; Yang, J.; Yu, Y.; Chen, S.; Qin, Y. Simultaneous Ni nanoparticles decoration and Ni doping of CdS nanorods for synergistically promoting photocatalytic H₂ evolution. *Appl. Surf. Sci.* 2020, **508**, 144869.
28. Saeed, S.; Siddique, H.; Dai, R.; Wang, J.; Ali, A.; Gao, C.; Tao, X.; Wang, Z.; Ding, Z.; Zhang, Z. Enhanced PEC Water Splitting Performance of Silver Nanoparticle-Coated CdS Nanowire Photoanodes: The Role of Silver Deposition. *J. Phys. Chem. C* 2021, **125**, (14), 7542-7551.
29. Yan, H.; Yang, J.; Ma, G.; Wu, G.; Zong, X.; Lei, Z.; Shi, J.; Li, C. Visible-light-driven hydrogen production with extremely high quantum efficiency on Pt–PdS/CdS photocatalyst. *J. Catal.* 2009, **266**, (2), 165-168.
30. Ye, A.; Fan, W.; Zhang, Q.; Deng, W.; Wang, Y. CdS–graphene and CdS–CNT nanocomposites as visible-light photocatalysts for hydrogen evolution and organic dye degradation. *Catal. Sci. Technol.* 2012, **2**, (5), 969-978.
31. Wang, J.; Li, Y.; Shen, Q.; Izuishi, T.; Pan, Z.; Zhao, K.; Zhong, X. Mn doped quantum dot sensitized solar cells with power conversion efficiency exceeding 9%. *J. Mater. Chem. A* 2016, **4**, (3), 877-886.
32. He, B.; Liu, R.; Ren, J.; Tang, C.; Zhong, Y.; Hu, Y. One-Step Solvothermal Synthesis of Petal-like Carbon-Coated Cu⁺-Doped CdS Nanocomposites with Enhanced Photocatalytic Hydrogen Production. *Langmuir* 2017, **33**, (27), 6719-6726.
33. Dong, Y.; Choi, J.; Jeong, H.-K.; Son, D. H. Hot Electrons Generated from Doped Quantum Dots via Upconversion of Excitons to Hot Charge Carriers for Enhanced Photocatalysis. *J. Am. Chem. Soc.* 2015, **137**, (16), 5549-5554.
34. Dong, Y.; Parobek, D.; Rossi, D.; Son, D. H. Photoemission of Energetic Hot Electrons Produced via Up-Conversion in Doped Quantum Dots. *Nano Lett.* 2016, **16**, (11), 7270-7275.
35. Jo, D.-Y.; Kim, D.; Kim, J.-H.; Chae, H.; Seo, H. J.; Do, Y. R.; Yang, H. Tunable White Fluorescent Copper Gallium Sulfide Quantum Dots Enabled by Mn Doping. *ACS Appl. Mater. Interfaces* 2016, **8**, (19), 12291-12297.
36. Dehnel, J.; Barak, Y.; Meir, I.; Budniak, A. K.; Nagvenkar, A. P.; Gamelin, D. R.; Lifshitz, E. Insight into the Spin Properties in Undoped and Mn-Doped CdSe/CdS-Seeded Nanorods by Optically Detected Magnetic Resonance. *ACS Nano* 2020, **14**, (10), 13478-13490.
37. Yang, Y.; Chen, O.; Angerhofer, A.; Cao, Y. C. On Doping CdS/ZnS Core/Shell Nanocrystals with Mn. *J. Am. Chem. Soc.* 2008, **130**, (46), 15649-15661.
38. Liu, M.; Du, Y.; Ma, L.; Jing, D.; Guo, L. Manganese doped cadmium sulfide nanocrystal for hydrogen production from water under visible light. *Int. J. Hydrogen Energy* 2012, **37**, (1), 730-736.
39. Li, Z.-J.; Li, S.; Davis, A. H.; Hofman, E.; Leem, G.; Zheng, W. Enhanced singlet oxygen generation by hybrid Mn-doped nanocomposites for selective photo-oxidation of benzylic alcohols. *Nano Res.* 2020, **13**, (6), 1668-1676.
40. Saunders, A. E.; Ghezellash, A.; Sood, P.; Korgel, B. A. Synthesis of High Aspect Ratio Quantum-Size CdS Nanorods and Their Surface-Dependent Photoluminescence. *Langmuir* 2008, **24**, (16), 9043-9049.
41. Habas, S. E.; Yang, P.; Mokari, T. Selective Growth of Metal and Binary Metal Tips on CdS Nanorods. *J. Am. Chem. Soc.* 2008, **130**, (11), 3294-3295.
42. Xu, Y.-N.; Ching, W. Y. Electronic, optical, and structural properties of some wurtzite crystals. *Phys. Rev. B* 1993, **48**, (7), 4335-4351.
43. Mardix, S.; Alexander, E.; Brafman, O.; Steinberger, I. T. Polytype families in zinc sulphide crystals. *Acta Crystallogr.* 1967, **22**, (6), 808-812.
44. Tian, J.; Lv, L.; Fei, C.; Wang, Y.; Liu, X.; Cao, G. A highly efficient (>6%) Cd_{1-x}Mn_xSe quantum dot sensitized solar cell. *J. Mater. Chem. A* 2014, **2**, (46), 19653-19659.
45. Yost, A. J.; Ekanayaka, T. K.; Gurung, G.; Rimal, G.; Horoz, S.; Tang, J.; Paudel, T.; Chien, T. Influence of the Cation on the Surface Electronic Band Structure and Magnetic Properties of Mn:ZnS and Mn:CdS Quantum Dot Thin Films. *J. Phys. Chem. C* 2019, **123**, (40), 24890-24898.
46. You, D.; Pan, B.; He, Y.; Wang, X.; Su, W. Enhanced visible light photocatalytic H₂ evolution over CeO₂ loaded with Pt and CdS. *Res. Chem. Intermed.* 2017, **43**, (9), 5103-5112.
47. Liu, S.; Guo, Z.; Qian, X.; Zhang, J.; Liu, J.; Lin, J. Sonochemical deposition of ultrafine metallic Pt nanoparticles on CdS for efficient photocatalytic hydrogen evolution. *Sustainable Energy & Fuels* 2019, **3**, (4), 1048-1054.
48. Park, H.; Kim, Y. K.; Choi, W. Reversing CdS Preparation Order and Its Effects on Photocatalytic Hydrogen Production of CdS/Pt-TiO₂ Hybrids Under Visible Light. *J. Phys. Chem. C* 2011, **115**, (13), 6141-6148.
49. Davis, A. H.; Hofman, E.; Chen, K.; Li, Z.-J.; Khammang, A.; Zamani, H.; Franck, J. M.; Maye, M. M.; Meulenberg, R. W.; Zheng, W. Exciton Energy Shifts and Tunable Dopant Emission in Manganese-Doped Two-Dimensional CdS/ZnS Core/Shell Nanoplatelets. *Chem. Mater.* 2019, **31**, (7), 2516-2523.
50. Bradshaw, L. R.; Hauser, A.; McLaurin, E. J.; Gamelin, D. R. Luminescence Saturation via Mn²⁺–Exciton Cross Relaxation in Colloidal Doped Semiconductor Nanocrystals. *J. Phys. Chem. C* 2012, **116**, (16), 9300-9310.
51. Cao, X.; Zheng, X.; Tian, J.; Jin, C.; Ke, K.; Yang, R. Cobalt Sulfide Embedded in Porous Nitrogen-doped Carbon as a Bifunctional Electrocatalyst for Oxygen Reduction and Evolution Reactions. *Electrochim. Acta* 2016, **191**, 776-783.
52. Hofman, E.; Khammang, A.; Wright, J. T.; Li, Z.-J.; McLaughlin, P. F.; Davis, A. H.; Franck, J. M.; Chakraborty, A.; Meulenberg, R. W.; Zheng, W. Decoupling and Coupling of the Host–Dopant Interaction by Manipulating Dopant Movement in Core/Shell Quantum Dots. *J. Phys. Chem. Lett.* 2020, **11**, (15), 5992-5999.
53. Zheng, W.; Wang, Z.; Van Tol, J.; Dalal, N. S.; Strouse, G. F. Alloy Formation at the Tetrapod Core/Arm Interface. *Nano Lett.* 2012, **12**, (6), 3132-3137.

54. Zheng, W.; Wang, Z.; Wright, J.; Goundie, B.; Dalal, N. S.; Meulenbergh, R. W.; Strouse, G. F. Probing the Local Site Environments in Mn: CdSe Quantum Dots. *J. Phys. Chem. C* 2011, **115**, (47), 23305-23314.
55. Kalisman, P.; Kauffmann, Y.; Amirav, L. Photochemical oxidation on nanorod photocatalysts. *J. Mater. Chem. A* 2015, **3**, (7), 3261-3265.
56. Wang, Z.; Meijerink, A. Concentration Quenching in Upconversion Nanocrystals. *J. Phys. Chem. C Nanomater. Interfaces* 2018, **122**, (45), 26298-26306.
57. Cao, J.; Yang, J.; Zhang, Y.; Yang, L.; Wang, Y.; Wei, M.; Liu, Y.; Gao, M.; Liu, X.; Xie, Z. Optimized doping concentration of manganese in zinc sulfide nanoparticles for yellow-orange light emission. *J. Alloys Compd.* 2009, **486**, (1-2), 890-894.
58. Choi, J. Y.; Park, W.-W.; Park, B.; Sul, S.; Kwon, O.-H.; Song, H. Optimal Length of Hybrid Metal-Semiconductor Nanorods for Photocatalytic Hydrogen Generation. *ACS Catal.* 2021, **11**, (21), 13303-13311.